Journal of Computational Physics **180,** 471–496 (2002)
doi:10.1006/jcph.2002.7092

Numerical Simulation of Dendritic Solidification with Convection: Two-Dimensional Geometry

Nabeel Al-Rawahi* and Gretar Tryggvason†

**Department of Mechanical Engineering, University of Michigan, Ann Arbor, Michigan 48109-2121; and*
†Mechanical Engineering Department, Worcester Polytechnic Institute, Worcester, Massachusetts 01609
E-mail: gretar@wpi.edu

Received September 5, 2001; revised April 26, 2002

A front tracking method is presented for simulations of dendritic growth of pure substances in the presence of flow. The liquid–solid interface is explicitly tracked and the latent heat released during solidification is calculated using the normal temperature gradient near the interface. A projection method is used to solve the Navier–Stokes equations. The no-slip condition on the interface is enforced by setting the velocities in the solid phase to zero. The method is validated through a comparison with an exact solution for a Stefan problem, a grid refinement test, and a comparison with a solution obtained by a boundary integral method. Three sets of two-dimensional simulations are presented: a comparison with the simulations of Beckermann *et al.* (*J. Comput. Phys.* **154**, 468, 1999); a study of the effect of different flow velocities; and a study of the effect of the Prandtl number on the growth of a group of dendrites growing together. The simulations show that on the upstream side the dendrite tip velocity is increased due to the increase in the temperature gradient and the formation of side branches is promoted. The flow has the opposite effect on the downstream side. The results are in good qualitative agreement with published experimental results, even though only the two-dimensional aspects are examined here.

1. INTRODUCTION

The formation of microstructures during solidification plays a major role in determining the properties of nearly all man-made metal products. Dendritic microstructures result from undercooling of the melt and are particularly common in binary alloys, where variable solute concentration can lead to localized constitutional undercooling. However, undercooling of a pure material can also lead to dendritic microstructure. Experimental results show that melt flow can have a significant impact on microstructure formation (Glicksman and Huang [1]) and in this paper we develop a numerical method for the simulation of two-dimensional dendrites in the presence of flow. Only pure materials are considered.

0021-9991/02 $35.00

Analytical solutions for dendritic growth are limited to very simple situations and numerical simulations are playing an increasing role in studies of dendrites. Early computations of the large-amplitude evolution include the boundary integral method of Strain [2], the level set simulations of Sethain and Strain [3], and the phase-field simulations of Wheeler *et al*. [4]. A variational algorithm was used by Almgren [5], and front tracking simulations were presented by Juric and Tryggvason [6]. Simulations of the growth of two-dimensional dendrites in a pure metal, in the absence of flow, have now become relatively common. A few three-dimensional computations have also been presented in the literature, including phase-field simulations by Kobayashi [7] and Karma and Rappel [8], finite element simulations by Schmidt [9], and a combined phase-field/Monte Carlo method by Plapp and Karma [10].

In the simulations listed above, the melt is assumed to be stationary. Phase-field methods have been extended to simulate the growth of two-dimensional dendrites with melt flow by Tonhardt and Amberg [11] and Beckermann *et al*. [12]. Tonhardt and Amberg studied the effect of shear flow on dendritic growth and modeled the solid as a fluid that was 100 times more viscous than the melt. Beckermann *et al.* examined the growth of a single dendrite in a uniform flow and held the solid in place by a force field added to the momentum equations. Finite element simulations were presented by Bansch and Schmidt [13], who modeled the solid and the fluid domain using separate grids and explicitly enforced the no-slip boundary condition at the interface. Juric [14] and Shin and Juric [15] presented front tracking simulations of the effect of shear flow on dendritic growth. They used an iterative scheme to calculate the heat source and advance the front and modeled the solid as a fluid with a viscosity that was 100 times that of the liquid. Here we develop a front tracking method to simulate the effect of convection on dendritic growth.

Simulations of dendritic growth with fluid flow require the incorporation of solid boundaries into the solution of the Navier–Stokes equations. Although the most accurate results are generally obtained when it is possible to align the grid to the interface by using a body-fitted grid, near a half century of CFD has shown that it is very hard to beat rectangular-structured grids in terms of simplicity and efficiency. When such grids are used, curved boundaries are not aligned with grid lines. One of the first papers to deal explicitly with how to include curve boundaries on rectangular grids is Viecelli [16], who simply approximated curved boundaries by the closest cell edges and applied a pressure to the boundary so that the normal velocity component was eliminated. More recently, Goldstein *et al.* [17] used a regularized singular force to hold the boundary in place. The force is added to the momentum equations and the strength of the force is adjusted iteratively. Saiki and Biringen [18] proposed an improved scheme, where the forces are predicted from the history of the motion, using control theory. Recent papers on the inclusion of curved boundaries on rectangular-structured grids include those of Lai and Peskin [19], Beckermann *et al.* [12], and Fadlun *et al.* [20]. Lai and Peskin pin the boundaries in place using linear springs, allowing small displacement, whereas Beckermann *et al.* compute the forces from the phase-field variable. Fadlun *et al.* pointed out that the forces can be found directly, thus reducing the computational effort considerably. In the papers discussed above, the effect of the immersed boundary is approximated by a distribution of forces on the fixed grid. This results in a finite thickness of the boundary, which must be smaller than any resolved length scale. To eliminate this smoothing, Ye *et al.* [21] represented the immersed boundary by a series of linear segments forming trapezoidal-shaped control volumes along the interface. Udaykumar *et al.* [22] extended the method of Ye *et al.* to allow for the motion of the immersed boundaries.

In the next section we present the mathematical formulation of the problem and the relevant nondimensional numbers. The implementation of the method is then described. The validation section includes a comparison with an exact solution for a Stefan problem, a grid refinement test, and a comparison with a solution obtained by a boundary integral method [23]. After validating the method, we present three sets of simulations in the results section: a comparison with the simulation of Beckermann *et al.*; a study of the effect of different flow velocities; and a study of the effect of the Prandtl number on the growing of a group of dendrites growing together. The last section contains a few concluding comments.

2. FORMULATION

The problem setup is sketched in Fig. 1. Undercooled liquid enters through the left boundary of a rectangular domain and flows past a dendrite in the center. As the liquid solidifies and the dendrite grows, the geometry of the solid/liquid boundary changes. The whole domain is resolved by a single fixed grid and one set of equations is used for both the liquid and the solid. The phase boundary is treated as an imbedded interface by adding the appropriate source terms as delta functions to the conservation laws. The temperature is found by solving the energy equation

$$\frac{\partial \rho c_p T}{\partial t} + \nabla \cdot (\rho c_p T \mathbf{u}) = \nabla \cdot k \nabla T + \int_F \dot{q} \delta(\mathbf{x} - \mathbf{x}_f)\, da, \tag{1}$$

where we have assumed that the fluid is incompressible and that viscous heating can be neglected. $\mathbf{u}$ is the fluid velocity (equal to zero in the solid), ρ and c_p are the density and heat capacity, respectively, k is the thermal conductivity, and $\mathbf{x}_f$ is the front location. The integral term is the heat liberated during solidification and the source strength $\dot{q}$ is related

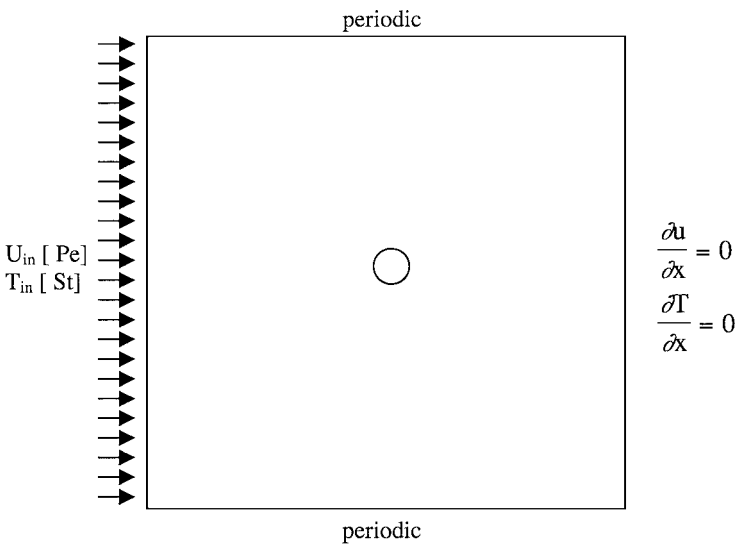

FIG. 1. The initial setup used in most of the simulations presented in this paper. A dendrite seed is located at the center of the domain and uniform undercooled liquid enters through the left boundary with a velocity determined by the Peclet number. Weak conditions are imposed on the outlet flow and periodic boundary conditions are used for the upper and lower boundaries.

to the normal velocity of the phase boundary V_n and the latent heat L by

$$\dot{q} = \rho L V_n. \tag{2}$$

The motion of the phase boundary is found by integrating

$$\frac{d\mathbf{x}_f}{dt} = V_n \mathbf{n}, \tag{3}$$

where $\mathbf{n}$ is the normal vector to the phase boundary. The heat source is determined in such a way that the interface temperature satisfies the Gibbs–Thompson relation

$$T_f = T_m \left(1 - \frac{\gamma}{\rho L}\kappa\right) - \frac{V_n}{\eta}. \tag{4}$$

Here, γ is the surface tension, η is the kinetic mobility, and κ is the curvature. The surface tension and the kinetic mobility are generally anisotropic and we use for the anisotropy the expression (see, for example, [11, 12, 24])

$$\begin{aligned} \gamma &= \gamma_o(1 - A_s \cos(m(\theta - \theta_o)), \\ \frac{1}{\eta} &= \frac{1}{\eta_o}(1 - A_k \cos(m(\theta - \theta_o)). \end{aligned} \tag{5}$$

Here, A_s and A_k are the anisotropy of the surface tension and the inverse of the kinetic mobility, respectively; θ is the angle of the normal to the interface; θ_o is the angle of the symmetry axis with respect to the x axis; and m determines the number of axes of symmetry for the dendrite. In the simulations presented in this paper we use $m = 4$ and $\theta_o = 0^\circ$ unless otherwise stated. This results in a dendrite with four axes of symmetry aligned with the x and the y axis.

The fluid motion is determined by the Navier–Stokes equations

$$\frac{\partial \mathbf{u}_{liquid}}{\partial t} + \nabla \cdot \mathbf{u}_{liquid}\mathbf{u}_{liquid} = -\nabla p + \nu \nabla^2 \mathbf{u}_{liquid} \tag{6}$$

and the velocity in the solid is zero,

$$\mathbf{u}_{solid} = 0. \tag{7}$$

Here, ν is the kinematic viscosity and p is the pressure. The fluid is assumed to be incompressible and the density of the solid and the liquid are assumed to be the same. Thermal convection due to changes in volume with temperature is therefore absent. Since the governing equations are solved on a single grid, we define a velocity field everywhere in the domain by

$$\mathbf{u} = \phi\, \mathbf{u}_{liquid}. \tag{8}$$

$\phi(x, y)$ is an indicator function that is given by

$$\phi = \begin{cases} 0 & \text{in the solid} \\ 1 & \text{in the liquid} \end{cases} \tag{9}$$

and varies smoothly between zero and one in the interface region. The mass conservation equation for the whole domain reduces to

$$\nabla \cdot \mathbf{u} = 0. \tag{10}$$

The thermal conductivity and the specific heat of each phase are assumed to be constant in each phase.

Before describing the algorithm used to solve the governing equations, it is useful to write down the governing nondimensional numbers. By defining a reference temperature $\tilde{T} = \frac{L}{c_{\mathrm{p,solid}}}$, a capillary length scale $d_{\mathrm{o}} = \frac{T_{\mathrm{m}}\gamma_{\mathrm{o}}c_{\mathrm{p,solid}}}{\rho L^2}$, and a time scale $\tau = d_{\mathrm{o}}^2(\frac{\rho c_{\mathrm{p,solid}}}{k_{\mathrm{solid}}})$, it is possible to show that for the solidification of a pure material in the absence of flow, there is only one nondimensional number if the material properties of the solid and the melt are the same and if surface tension anisotropy and kinetic effects are neglected. This number is usually taken to be the nondimensional undercooling $\mathrm{St} = \frac{c_{\mathrm{p,solid}}\Delta T}{L}$, or the Stefan number. Notice that the surface tension and the thermal conductivity do not appear explicitly in this group. These variables simply set the length and time scale of the evolution, but do not otherwise affect the results. In the general case, it is also necessary to specify the ratios of the material properties, the anisotropy of the surface tension and kinetic mobility, and the nondimensional kinetic mobility, i.e., $k_{\mathrm{liquid}}/k_{\mathrm{solid}}$, $c_{\mathrm{p,liquid}}/c_{\mathrm{p,solid}}$, A_{s}, A_{k}, and $\frac{k_{\mathrm{solid}}}{\eta_{\mathrm{o}}Ld_{\mathrm{o}}}$. When fluid flow is added, the flow Peclet number and the Prandtl number must also be specified. If the capillary length d_{o} is used in the definition of the flow Peclet number, those are

$$\mathrm{Pe_f} = \frac{k_{\mathrm{solid}}Ud_{\mathrm{o}}}{c_{\mathrm{p,solid}}} \quad \text{and} \quad \mathrm{Pr} = \frac{k_{\mathrm{solid}}}{c_{\mathrm{p,sloid}}\mu}.$$

3. NUMERICAL IMPLEMENTATION

The energy equation and the momentum equation are solved on a fixed grid that covers both the liquid and the solid region. The phase boundary is represented by moving marker points, connected to form a one-dimensional front that lies on the two-dimensional stationary mesh. The front is used to advect the discontinuous material property fields and to calculate the heat source. The energy equation and the momentum equations are discretized using a conservative, second-order, centered difference scheme for the spatial variables and an explicit second-order predictor–corrector time integration scheme. For details of the discretization, see [25]. A uniform inflow with temperature equal to the undercooling temperature is specified on the left boundary of the computational domain, the top and bottom of the domain are periodic, and the fluid is allowed to flow freely out through the right boundary by using Neumann boundary conditions for both the velocity and the temperature.

To maintain stability the time step is bounded by four criteria: from the heat equation by $\Delta t \leq h^2/4/(k/\rho c_{\mathrm{p}})$, from the Navier–Stokes equation by $\Delta t \leq 4\nu/U^2$ and $\Delta t \leq h^2/(4\nu)$, and from constraining the front from moving no more than a fraction of the grid spacing in each time step by $\Delta t \leq h/(4V)$. The most restrictive conditions are given by the first and the third criterion.

To find the heat source and thus the velocity of the phase boundary or the front, we integrate the energy equation across the phase boundary. The result is that the heat released

by the motion of the front must be balanced by heat conduction away from the front:

$$\dot{q} = k_{\text{solid}} \frac{\partial T}{\partial \mathbf{n}}\Big)_{\text{solid}} - k_{\text{liquid}} \frac{\partial T}{\partial \mathbf{n}}\Big)_{\text{liquid}}. \tag{11}$$

To estimate the temperature gradients on either side of the front, we draw the normal to the front and find points at $\omega^* h$ away from the front,

$$\begin{aligned} x^{\pm} &= x_1 \pm \omega h(\Delta y)/\Delta s, \\ y^{\pm} &= y_1 \pm \omega h(-\Delta x)/\Delta s, \end{aligned} \tag{12}$$

where the plus (+) sign applies to the right hand side, i.e., the liquid side, and the minus (−) sign applies to the left hand side, i.e., the solid side. Here h is the grid spacing, and ω is an adjustable parameter. $\omega = 1.2$ was found to give the highest accuracy, as discussed in the validation section. Here,

$$\begin{aligned} \Delta x &= x_2 - x_0, \\ \Delta y &= y_2 - y_0, \\ \Delta s &= \sqrt{(x_2 - x_0)^2 + (y_2 - y_0)^2} \end{aligned} \tag{13}$$

(see Fig. 2 for the notation used). The temperature at $(x^{\pm}, y^{\pm})$ is found from the grid temperature using an area-weighing interpolation function and the heat source is estimated by

$$\dot{q} = \frac{1}{\omega h}(k_{\text{s}}(T_- - T_{\text{f}}) - k_{\text{l}}(T_{\text{f}} - T_+)). \tag{14}$$

Here, T_{f} is the temperature at the front, given by Eq. (4). We have also experimented with higher order approximations, where we find two points on either side, a distance $\omega^* h$ and $2^*\omega^* h$ from the front, and fit a quadratic polynomial to estimate the gradient at the front. However, the results from using a linear fit were found to be in a better agreement with

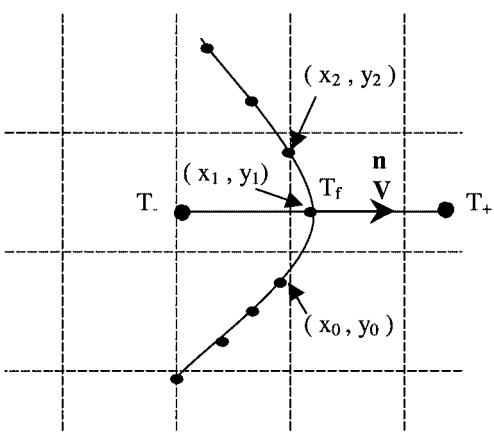

FIG. 2. The fixed and the moving grid with points used to calculate the normal temperature gradient across the front for one point on the moving grid.

the exact solutions, as shown in the validation section. The curvature, needed in Eq. 4, is found by fitting two-third order polynomials through each point and taking the average of the two values calculated from these polynomials. One polynomial is fitted using two points from one side and one from the other side. The other polynomial is found by switching the sides with two and one point. Once the heat source is found, the location of the interface is updated by integrating Eq. (3) using a second-order, predictor–corrector method. The heat source found by Eq. (4) is distributed onto the fixed grid by Peskin's cosine function [26].

The indicator function ϕ is constructed from the front location by distributing the jump in ϕ onto the fixed grid and integrating it by solving a Poisson equation. This results in a field that has the correct values in the solid and the liquid and a smooth transition zone across the front. The width depends on the function used to distribute the jump onto the grid. In the computations presented here, we use Peskin's cosine function, which results in a zone about five mesh-spacings wide.

The main challenge in solving the momentum equations is the enforcement of a zero velocity in the solid. As discussed in the Introduction, several authors have represented solid boundaries on fixed grids by finding the forces needed to hold them in place. Generally, it is necessary to use an iterative method to find the force. However, it has recently become clear that the computations can be simplified with minimal loss of accuracy (see Fadlun *et al.* [20] for example) by simply setting the velocity in the solid to zero (if the solid is stationary). This can be accomplished by a slight modification of the standard projection scheme. First we split the Navier–Stokes equations in the usual way and then multiply the unprojected velocity, $\mathbf{u}^*$, and the pressure gradient by ϕ to set the velocity in the solid to zero:

$$\mathbf{u}^* = \phi(\mathbf{u}^n + \Delta t\, \mathbf{A}(\mathbf{u}^n)), \tag{15}$$

$$\mathbf{u}^{n+1} = \mathbf{u}^* - \Delta t\, \phi \nabla P. \tag{16}$$

Here, $\mathbf{A}$ is the discrete advection and diffusion term in the Navier–Stokes equations. The new velocity field should be divergence free,

$$\nabla \cdot \mathbf{u}^{n+1} = 0, \tag{17}$$

and to see whether this is satisfied we note first that Eq. (15) is equivalent to

$$\mathbf{u}^{n+1} = \phi(\mathbf{u}^{**}), \tag{18}$$

where $\mathbf{u}^{**} = \mathbf{u}^* - \Delta t \nabla P$. Expanding the divergence yields

$$\nabla \cdot \mathbf{u}^{n+1} = \nabla \cdot \phi \mathbf{u}^{**} = \phi \nabla \cdot \mathbf{u}^{**} + \mathbf{u}^{**} \cdot \nabla \phi = 0. \tag{19}$$

Generally, the normal velocity at the phase boundary is small and the last term can be ignored. It is therefore usually sufficient to solve only

$$\nabla \cdot \mathbf{u}^{**} = 0. \tag{20}$$

This approximation makes the computations essentially identical to standard projection methods without any solid region. If $\mathbf{u}^{**} \cdot \nabla \phi$ is not small, an iteration would be necessary.

We have also found that instead of using the index function ϕ directly, using ϕ^2 helps keep the phase boundary sharper. This is similar to the use of nonsymmetric weighting by Beckermann *et al.* [12]. A test of how well this approach works for a well-defined geometry is presented in the validation section of this paper.

As the topology of the phase boundary changes, it is necessary to add and delete points to maintain a smooth representation of the front. To do this, we monitor the separation between the points and add or delete points if the separation exceeds specified maximum or minimum values, respectively. To keep the front smooth, the location of new points is determined by fitting a cubic polynomial through the old points. Generally, the results are insensitive to the spacing of the front points, as long as there is one or more front points in each mesh block.

4. VALIDATION

To validate and check the code, we have conducted a number of tests. The solidification part has been checked separately by comparing the numerical results to analytical solutions for a two-dimensional Stefan problem and the flow solver is validated through a comparison with analytical solutions for Stokes flow through a square array of parallel cylinders. The convergence of the method is tested by grid refinement studies and results for growth without flow are compared with a solution obtained by a boundary integral method that represents an essentially exact solution for two-dimensional growth.

The solution for the Stefan problem is given by Carslaw and Jaeger [27]. For the solidification of an infinitely long cylinder with a heat sink in the center, the nondimensional temperature in the liquid phase is given by

$$T(r,t) = \mathrm{St}\left[1 - \frac{Ei\left(-\frac{\alpha_s r^2}{4\alpha_l t}\right)}{Ei\left(-\frac{\alpha_s \lambda^2}{\alpha_l}\right)}\right]. \tag{21}$$

In the solid phase the solution is

$$T(r,t) = \frac{Q_L}{4\pi}\left[Ei\left(\frac{-r^2}{4t}\right) - Ei(-\lambda^2)\right]. \tag{22}$$

The radius of the solid cylinder is given by

$$R_f(t) = 2\lambda t^{0.5}, \tag{23}$$

where λ is the root of

$$Q_L = 4\pi e^{\lambda^2}\left[\frac{-\mathrm{St}\, k_l e^{\alpha_s \lambda^2/\alpha_l}}{k_s Ei(-\alpha_s \lambda^2/\alpha_l)} + \lambda^2\right]. \tag{24}$$

The heat sink, Q_L, is modeled numerically by fixing the cylinder center in the center of a mesh block and keeping the temperature of the four corner points equal to the exact temperature. In Fig. 3a, where $\mathrm{St} = 1$, $Q_L = 10$, and $k_l/k_s = c_l/c_s = 1$, the exact and the average numerical radius calculated by averaging the radius of all front points of the interface

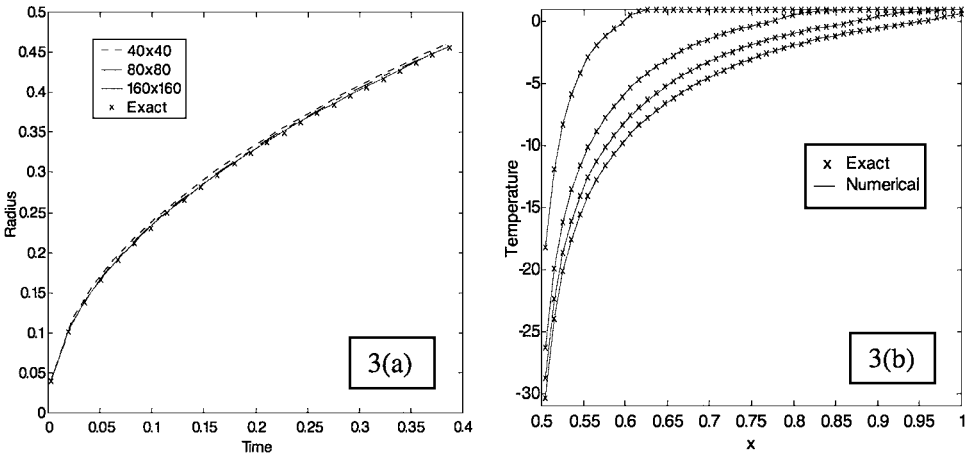

FIG. 3. Numerical and analytical results for the Stefan problem for the solidification of an infinitely long cylinder with a heat sink in the center. (a) With St $= 1$, $Q_{\mathrm{L}} = 10$, and $k_{\mathrm{l}}/k_{\mathrm{s}} = c_{\mathrm{l}}/c_{\mathrm{s}} = 1$, the radius of the interface for different grid resolutions and compared to the exact solution. (b) With St $= 1$, $Q_{\mathrm{L}} = 50$, $k_{\mathrm{l}}/k_{\mathrm{s}} = 0.2$, and $c_{\mathrm{l}}/c_{\mathrm{s}} = 1$, the numerical and the exact temperature profiles at the centerline of the domain at different time steps.

is shown for different grid resolutions. The numerical results are in a very good agreement with the exact solution and the error decreases as finer grids are used. The temperature profile at the centerline is plotted in Fig. 3b for St $= 1$, $Q_{\mathrm{L}} = 50$, $k_{\mathrm{l}}/k_{\mathrm{s}} = 0.2$, and $c_l/c_s = 1$. The result demonstrates the ability of the method to predict the temperature profile and to capture the jump in the temperature gradient across the interface.

To test the accuracy of the flow solver and the way solid boundaries are included, Stokes flow over a square arrays of parallel cylinders was simulated for different void fractions and the results compared to the analytical solutions of Drummond and Tahir [28] and Sangani and Acrivos [29]. The simulations were done for a large range of void fractions, but it should be noted that the analytical solutions are only valid for low void fractions. Figure 4 shows the flow field around a cylinder for void fraction equal to 0.12566. Here, all boundaries are periodic and the flow is driven by an imposed pressure gradient. Figure 5 shows the numerical results and the analytical solutions for the nondimensionalized mean velocity as a function of the void fraction. The numerical results are obtained using two grid resolutions and both show a very good agreement with the analytical solutions, in the region where the analytical solutions are valid. The numerical results do, in particular, converge on the analytical solutions as the grid resolution is refined.

Solutions using a boundary integral method provide another means for validating the numerical results. Such simulations can be made very accurate and give essentially exact solutions for two-dimensional growth. We compare our results for the growth without flow with the boundary integral solution reported by Karma and Rappel [23]. In this simulation St $= -0.55$, the inverse kinetic mobility is zero, and $A_{\mathrm{s}} = 0.75$. A 770^2 grid is used to resolve a domain that is 2161.151^2 nondimensional length units. The tip velocity reported by Karma and Rappel for the boundary integral method solution is 0.017. This problem was used to select the parameter ω in Eq. (12), to study the effect of using either linear or quadratic fit for the temperature near the interface when calculating the heat source, and to study the effect of using either Peskin's cosine interpolation function or the area-weighing

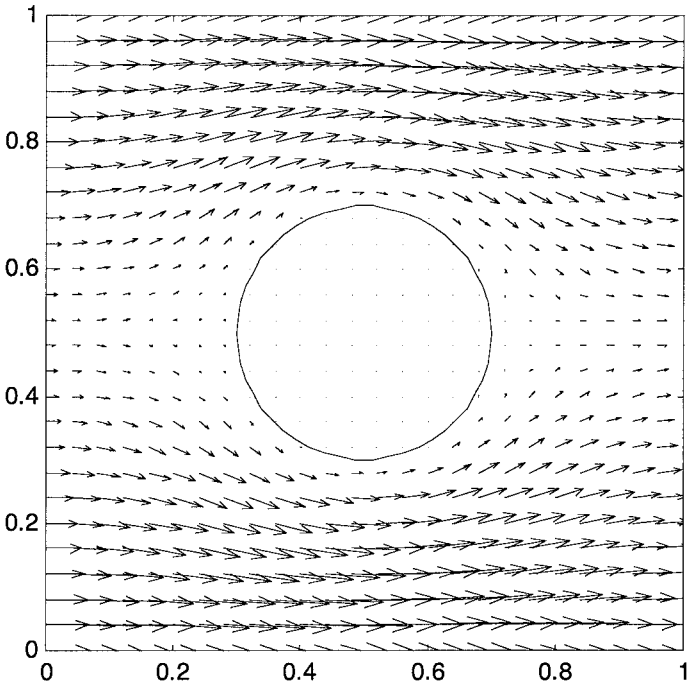

FIG. 4. The flow field around a cylinder of radius 0.2, which corresponds to a void fraction of 0.12566. All boundaries are periodic and the flow is driven by an imposed pressure gradient.

function in interpolating the temperature and in distributing the heat source found in Eq. (14). The parameter ω was varied between 0.6 and 1.6 for both linear and quadratic temperature profiles near the interface using different combinations for the interpolating functions. The linear temperature profile generally provided better results and was therefore chosen for the rest of the computations. The slight superiority of the linear profile is perhaps a little surprising and while we have not conducted a systematic study to determine the exact reason, we suspect that the reason is the smoothing of the interface and that we select the point that we use to compute the gradient as close to the interface as possible to avoid interference from other parts of the dendrite. If the temperature at this point is a little too low, then the quadratic fit will overestimate the gradient. The linear fit gives a slightly lower value (and hence is more correct in the sharp interface limit). Using three values of the parameter ω, 1.0, 1.2, and 1.4, the growth direction was rotated 45° to determine the effect of grid anisotropy on the results. The tip velocities from these tests were between 0.0164 and 0.0180. Table I shows the tip velocity obtained from these tests. The value of 1.2 was chosen because it agrees with the exact solution and is insensitive to the choice of the interpolating functions and the growth direction. The Peskin's cosine interpolation function was selected to distribute the heat source and the area-weighing function was selected to interpolate the temperatures for Eq. (14).

Since there are no theoretical results for the growth of a dendrite in a flow, a grid resolution test is presented to show how the results converge. The test was carried out using four grids, of 128^2, 256^2, 512^2, and 1024^2 grid points, in a domain of $(25.6 \times 10^3)^2$ nondimensional length units. The nondimensional parameters are $\mathrm{St} = -0.3$, $\mathrm{Pr} = 0.1$, $\mathrm{Pe_f} = 0.004$, zero inverse kinetic mobility, and an anisotropy of 40% of the surface tension. The computations

TABLE I

Results for the Dendrite Arm Tip Velocity for the Test Conducted to Select the Parameter ω

	Angle θ_o	$\omega = 1.0$	$\omega = 1.2$	$\omega = 1.4$
Using the Peskins cosine interpolation function for interpolating the temperatures and distributing the heat sources	0°	0.018	0.0171	0.0165
	45°	0.0181	0.0170	0.0167
Using the Peskins cosine interpolation function for interpolating the temperatures while using the area-weighing function for distributing the heat sources	0°	0.0174	0.0170	0.0166
	45°	0.0175	0.0170	0.0165
Using the area-weighing function for interpolating the temperatures while using the Peskins cosine interpolation function for distributing the heat sources	0°	0.0176	0.0170	0.0165
	45°	0.0179	0.0170	0.0163
Using the area-weighing function for interpolating the temperatures and distributing the heat sources	0°	0.0175	0.0170	0.0168
	45°	0.0171	0.0169	0.0164

Note. The parameters used in these simulations are St $= -0.55$, $A_s = 0.75$, zero inverse kinetic mobility, and equal material properties. A linear temperature profile was used to compute the heat sources at the interface. The tip velocity obtained from the boundary integral solution is equal to 0.0170.

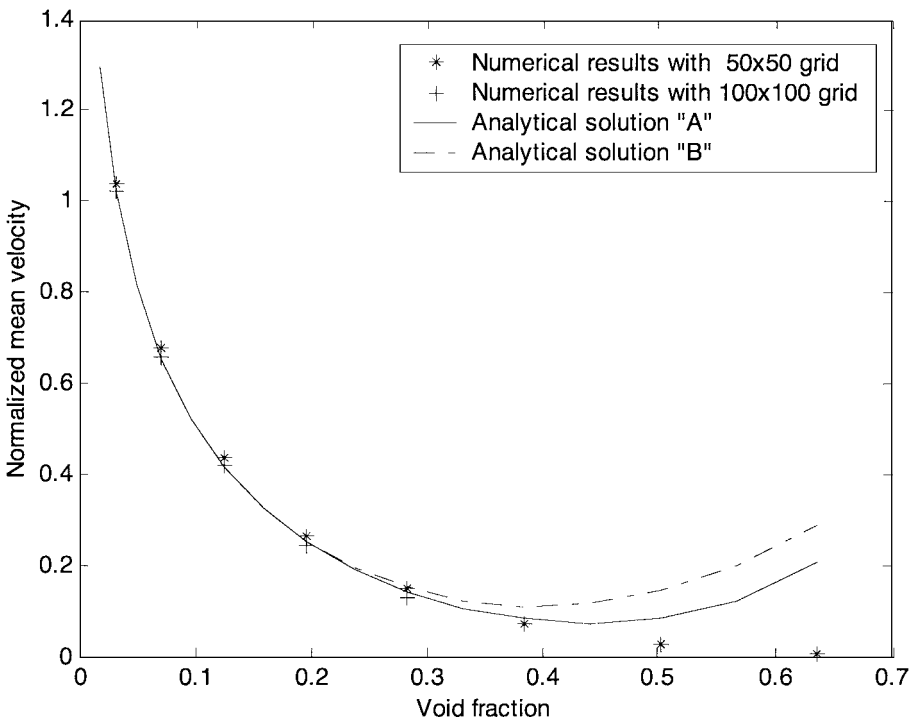

FIG. 5. Nnumerical results and the analytical solutions for the nondimensionalized mean velocity as a function of the void fraction. Two numerical results are shown using two grid resolutions and both show a very good agreement with the analytical solutions, in the region where the analytical solutions are valid. The numerical results converge to the analytical solution as the grid is refined. The analytical solutions "A" and "B" are obtained from Refs. [28, 29], respectively.

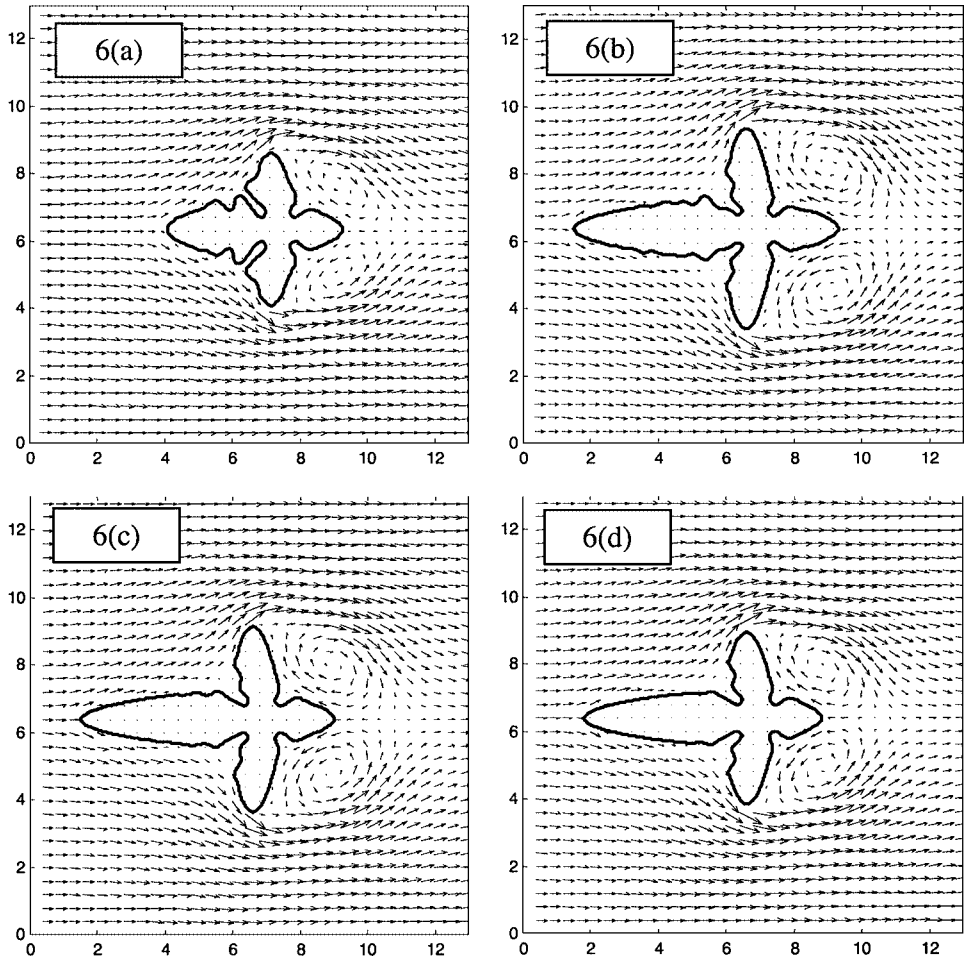

FIG. 6. Grid resolution test performed with the following parameter: St $= -0.3$, Pr $= 0.1$, Pe $= 0.004$, zero inverse kinetic mobility, and an anisotropy of 40% of the surface tension. (a–d) The interface and the velocity fields at a nondimensional time about 2.1×10^6 for the four grid resolutions used: 128^2, 256^2, 512^2, and 1024^2 grid points, respectively. The axis ranges are multiplied by 10^{-3}.

were started with a solid phase with a temperature equal to 0, surrounded by undercooled liquid metal. The initial solid radius is 500, with a fourfold perturbation in the interface shape of the type $\cos(4\theta)$. Figure 6 shows the interface and the velocities at a nondimensional time of about 2.1×10^6 for the four grid resolutions. While the result obtained using the first grid, 128^2, shows different behavior, the solutions from the three finer grids are almost identical. Figure 7 shows the tips velocities for the four grids. To make the figure more readable, the tip velocities of the arm growing perpendicular to the flow and the arms growing in the downstream direction are not shown for the two coarsest grids. The figure shows that when going from the 128^2 grid to the 256^2 grid the upstream tip velocity increased by about 50%, whereas the tip velocity only increased by about 12% between the 256^2 grid and the 512^2 grid. The upstream tip velocity obtained using the 1024^2 grid is essentially the same as for the 512^2 grid. These two finest grids also produce the same results for the downstream tip velocity and the velocity of the tip of the arms perpendicular to the flow.

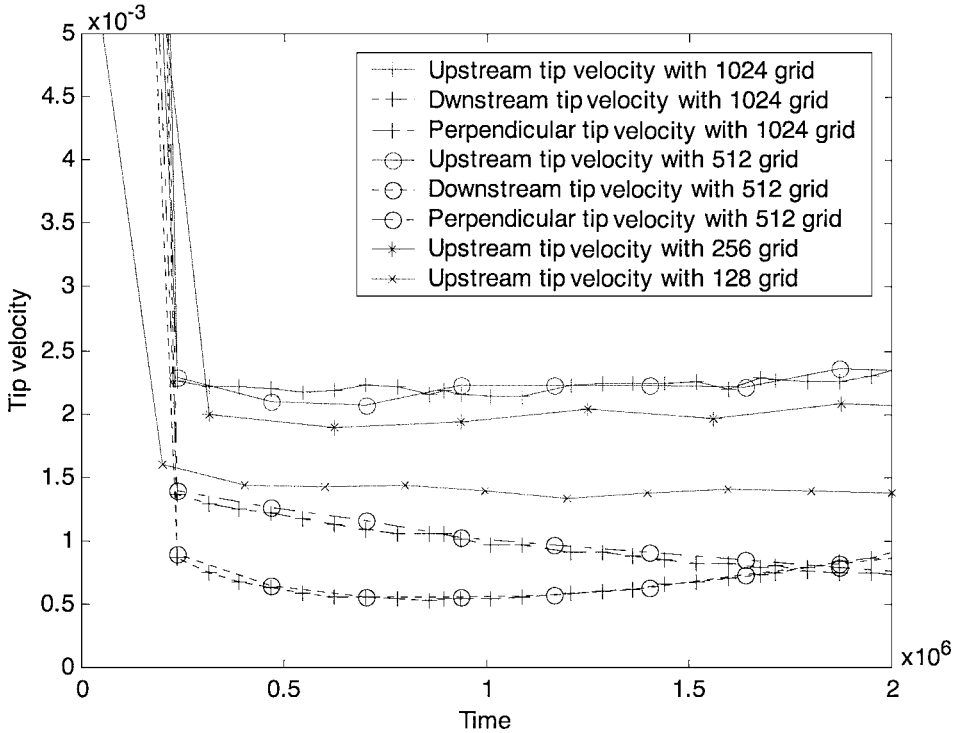

FIG. 7. Dendrite arms tip velocities from the grid resolution test presented in Fig. 6.

5. RESULTS

Three sets of simulations are presented here. The first one is a comparison with the results of Beckermann *et al.* The second set is a study of the effect of two different flow velocities on the dendritic growth. The third set is a study of the effect of the Prandtl number on the growth of many dendrites growing close to each other. The last example illustrates the ability of the code to deal with more that one dendrite. The results are compared to the growth without flow in all cases.

Although dendritic growth is a highly three-dimensional process, two-dimensional simulations are expected to give a reasonably accurate picture of the phenomenon and to capture various trends as the control parameters are changed. In particular, two-dimensional simulations should capture closely the behavior of the upstream tip, since it grows in an essentially axisymmetric way. The shortcoming of two-dimensional simulations is expected to be more obvious for the downstream arm and the arms growing perpendicular to the flow. This is because the flow in the two-dimensional simulations has to go around the tip of the arm growing perpendicular to the flow instead of going around its side. This may lead to early flow separation and a larger downstream wake.

5.1. *Comparison with the Results of Beckermann et al.*

We start by considering the simulations presented by Beckermann *et al.* and compare our results to theirs. The nondimensional parameters used in their simulations are the same as

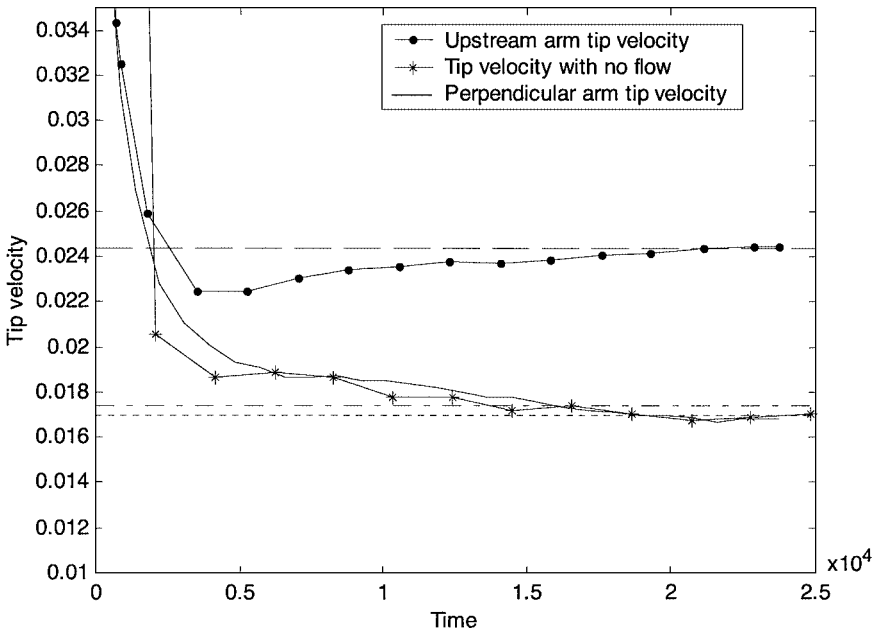

FIG. 8. Dendrite arms tip velocities with and without flow. The parameters used in these simulations are St $= -0.55$, Pr $= 23.1$, Pe $= 0.03475$, $A_s = 0.75$, zero inverse kinetic mobility, and equal material properties. The tip velocities from our simulations are compared to the steady state upstream arm tip velocity, 0.0244 (dash line, — — —) and the perpendicular arm tip velocity, 0.0174 (dash–dot line, —·—·) obtained from simulations of Beckerman *et al.*, and to the boundary integral solution of Karma and Rappel [23] for the velocity of the tip of the arm without flow, 0.0170 (dotted line, - - -).

the ones used in the comparison with the boundary integral solution. However, a flow field with $\mathrm{Pe_f} = 0.03475$ and Pr $= 23.1$ is added. Figure 8 shows the tips velocities compared to the tip velocity for growth without flow. The converged velocities for the tip of the upstream arm and the arm growing perpendicular to the flow are 0.0170 and 0.0244, respectively. The corresponding velocities from the simulations by Beckermann *et al.* are 0.0174 and 0.0244, respectively. The tip velocity of the downstream arm has not reached a steady state by the end of the simulation and keeps decreasing. This is also observed in the simulations of Beckermann *et al.* For the no-flow case Beckermann *et al.* found the tip velocity to be 0.0174. Table II shows the tip radii for growth with and without flow. For growth without

TABLE II
Average Tip Radii Calculated by Taking the Mean Values of Tip Radii from Time Equal to 1.4–2.1 $\times$ 10^4

Pe	Upstream tip radius	Downstream tip radius	Perpendicular tip radius
0		7.0	
0.03475	6.3	7.5	7.4

Note. The parameters used in these simulations are St $= -0.55$, Pr $= 23.1$, Pe $= 0.03475$, $A_s = 0.75$, zero inverse kinetic mobility, and equal material properties.

flow the value found here, 7.0, is in agreement with the value reported by Beckermann *et al.*, 6.88. However, the trend observed for the effect of flow on tip radii is quite different. In our simulation the upstream tip radius is lower than the tip radius without flow, whereas in the simulations presented by Beckermann *et al.* the upstream tip radius is found to be higher than the tip radius without flow. Experimental results show that the upstream tip radius decreases when flow is introduced [30], which is in agreement with our results.

5.2. *Peclet Number Effect*

To study the effect of different flow velocities on the growth of a single dendrite we use the following parameters: $\mathrm{St} = -0.35$, $A_s = 0.4$, $\mathrm{Pr} = 0.1$, zero inverse kinetic mobility, and equal material properties. The two flow Peclet numbers are $\mathrm{Pe_f} = 0.001$ and 0.002. The first Peclet number is equal to the local Peclet number based on the propagation velocity of the tip of the dendrite arm for growth without flow. These parameters do not correspond directly to any specific material and were selected in part to make the computations reasonably fast. The relatively high Stefan number was selected to delay the effect of the boundary condition and allow us to use a relatively small computational domain. The properties are, however, within the range of real material properties. For example, the Prandtl number for succinonitrile is 23.1 and for lead it is 0.027. In Fig. 9 we show the dendrite and the temperature contours around the dendrite at a nondimensional time equal to 3.15×10^6 for zero flow. The isotherms are shown for temperatures equal to -0.1, -0.15, -0.2, -0.25, -0.3, and -0.3465. The outer contour, -0.3465, represents the thermal boundary layer

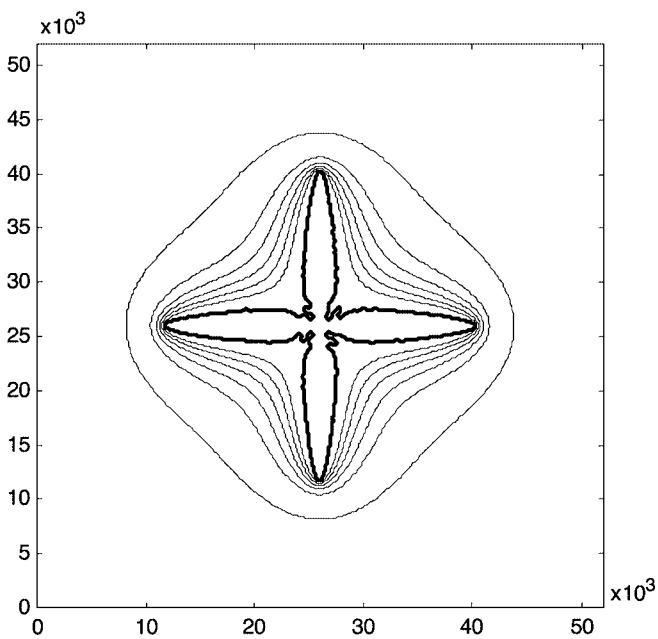

FIG. 9. Temperature contours around a dendrite at a nondimensional time equal to 3.15×10^6 for zero flow. The parameters used are $\mathrm{St} = -0.35$, $\mathrm{Pr} = 0.1$, $\mathrm{Pe} = 0.0$ (no flow), $A_s = 0.4$, zero inverse kinetic mobility, and equal material properties. The contour lines represent isotherms for temperatures equal to -0.1, -0.15, -0.2, -0.25, -0.3, and -0.3465. The outer contour, -0.3465, represents the thermal boundary layer defined as 99% of the undercooling.

defined as 99% of the undercooling. The dendrite grows symmetrically in the four preferred directions of growth and the temperature field is also symmetric.

For an inlet flow with $Pe_f = 0.001$, the frames in the left column of Fig. 10 show the temperature contours around a growing dendrite. Starting from the top of the figure, the nondimensional times are 3.15, 5.85, and 12.45×10^6. The temperature contour values are the same as in Fig. 9. The right column of Fig. 10 shows the velocity field around the dendrite at the same times. The effect of the flow on the temperature in the melt is shown clearly in these figures. Unlike the case of growth without flow, the temperature contours are not symmetric in all four directions. The flow compresses the thermal boundary layer near the tip of the arm growing in the upstream direction while expanding it on the downstream side. The thermal boundary layer thickness near the tip of the dendrite arm perpendicular to the flow is not affected much by the flow. As a result of the smaller thermal boundary layer thickness near the tip of the upstream arm, and therefore higher temperature gradient, its growth rate is increased. The growth rate of the downstream arm, on the other hand, is reduced because of the lower temperature gradient there. The perpendicular arm is shifted slightly toward the flow direction with no significant effect on its growth rate. The higher temperature gradient on the upstream side also promotes the growth of side branches while on the downstream side the lower temperature gradient provides more homogeneous temperature that inhibits the growth of side branches. Separation of flow on the downstream side is seen in the last frame. This might indicate that two-dimensional effects are starting to be significant, as discussed previously.

In Fig. 11 the inlet flow strength has been increased to $Pe_f = 0.002$. The frames in the left column of Fig. 11 show the temperature contours around a growing dendrite. Starting from the top of the figure, these contours are at nondimensional times of 3.15, 5.85, and 12.45×10^6. The isotherms are the same as in Fig. 9, with the outer contour representing the edges of the thermal boundary layer. The frames in the right column of Fig. 11 show the velocity field around the dendrite at the corresponding times. The upstream arm now grows faster and the flow separation on the downstream side starts earlier. This large wake has a significant effect on the temperature profile, as seen in the bottom frame. As the wake grows, the fluid starts to flow toward the tip of the downstream arm, resulting in an increase in the temperature gradient near the tip. On the upstream side, more and larger side branches are formed and the arm growing perpendicular to the flow is shifted more toward the incoming flow.

Figure 12 shows the velocities, represented as Peclet numbers, of the tips of the dendrites for the three simulations discussed above. With a flow Peclet number of 0.001 the upstream tip velocity is increased by about 70% compared to the no-flow case while the downstream tip velocity is reduced by about 65%. The tip velocity of the arm growing perpendicular to the flow is initially equal to the tip velocity for the no-flow case but then starts to decrease. A number of factors affect the tip velocity of this arm. As the upstream arm grows, more heat is released from the upstream side. This heat has to be carried by the flow around the tip of the perpendicular arm, which reduces the temperature gradient there. The backflow generated by the wake has a similar effect, but for the downstream side of the dendrite. In addition, there is an effect of the increasing difference between the actual growth direction of the tip, tilted toward the flow, and the preferred growth direction imposed by the anisotropy of the surface tension. With increased inlet velocity, the effect of flow on the tip velocities is stronger. The upstream tip velocity is increased by about 110% for $Pe_f = 0.002$ compared to the no-flow case. The higher upstream tip velocity, the larger wake on the downstream

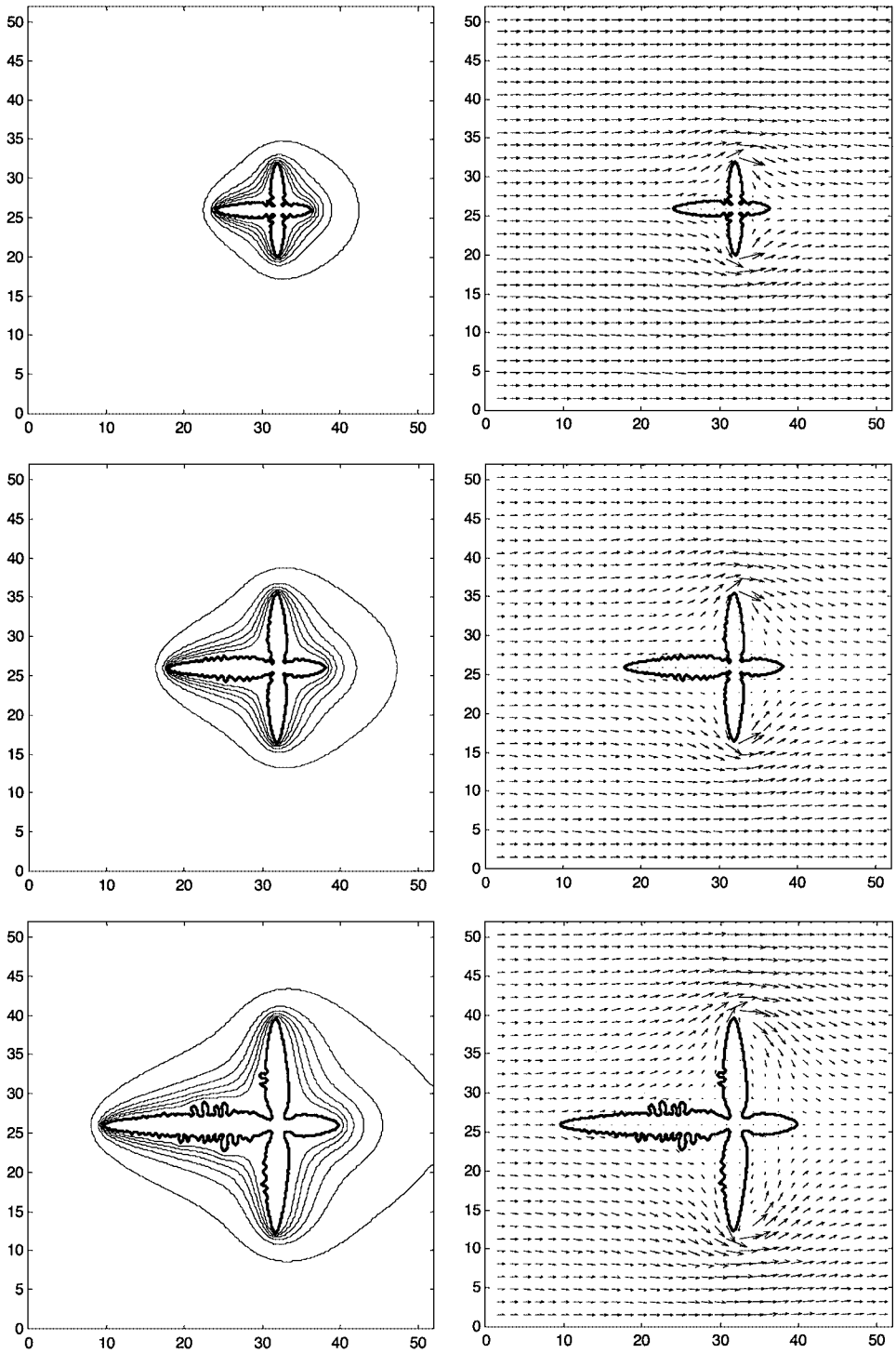

FIG. 10. Temperature and velocity fields around a dendrite at nondimensional times of 3.15, 5.85, and 12.45×10^6 (top, middle, and bottom, respectively). The parameters used are $\mathrm{St} = -0.35$, $\mathrm{Pr} = 0.1$, $\mathrm{Pe} = 0.001$, $A_s = 0.4$, zero inverse kinetic mobility, and equal material properties. The contour lines represent the same isotherms for temperature as used in Fig. 9. In the figure the axis values are multiplied by 10^{-3}.

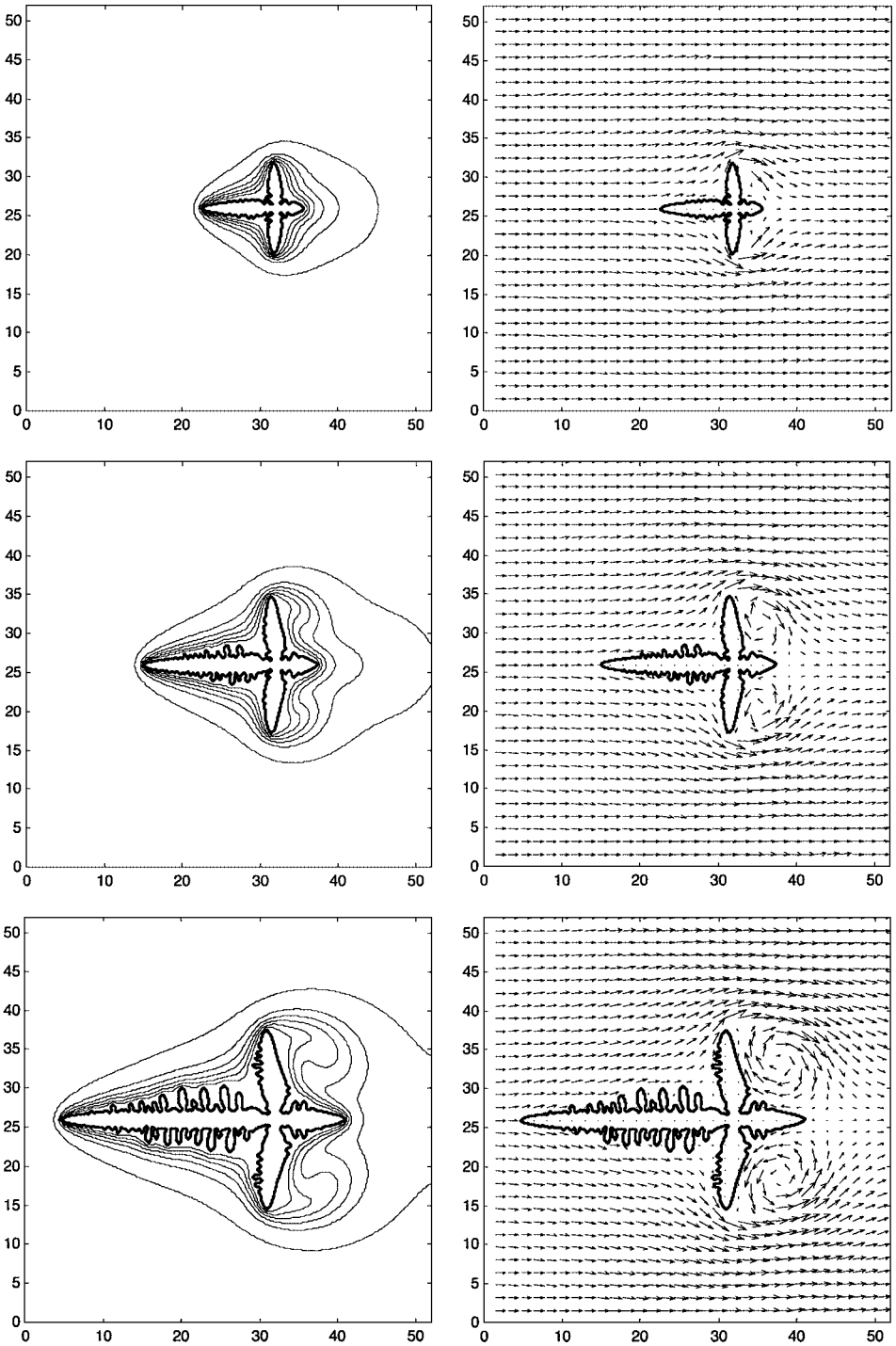

FIG. 11. Temperature and velocity fields around a dendrite at nondimensional times of 3.15, 5.85, and 12.45×10^6 (top, middle, and bottom, respectively). The parameters used are $\mathrm{St} = -0.35$, $\mathrm{Pr} = 0.1$, $\mathrm{Pe} = 0.002$, $A_s = 0.4$, zero inverse kinetic mobility, and equal material properties. The contour lines represent the same isotherms for temperature as used in Fig. 9. In the figure the axis values are multiplied by 10^{-3}.

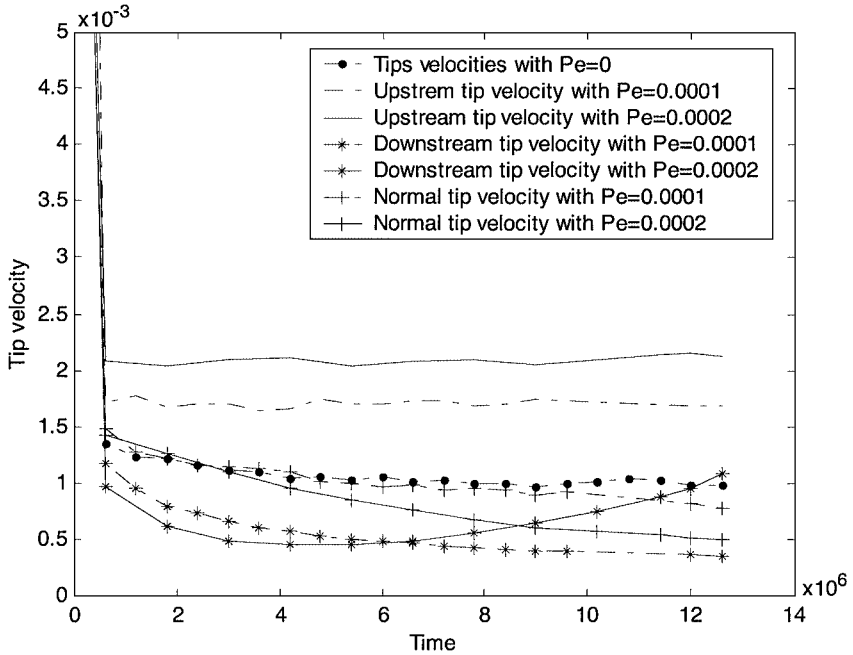

FIG. 12. The effect of the Peclet number on the dendrite arms tip velocities. The Peclet numbers used in the simulations are Pe = 0.0, 0.001, and 0.002. The other parameters used in these simulations are St = −0.35, Pr = 0.1, Pe = 0.0 (no flow), $A_s = 0.4$, zero inverse kinetic mobility, and equal material properties.

side, and the increased tilt of the perpendicular arm into the flow results in a larger reduction of its tip velocity. The growth velocity of the downstream arm increases significantly after decreasing initially. This is due to the change in the wake structure and the sharpening of the temperature gradient near the tip of the downstream arm. This was discussed when Fig. 11 was presented.

Table III shows the average radii, the Peclet number, $\mathrm{Pe_t} = (VR)_{\mathrm{tip}}$, and the stability parameter, $\sigma^* = 2/(VR^2)_{\mathrm{tip}}$, of the dendrite arms tips for $\mathrm{Pe_f} = 0, 0.001$, and 0.002

TABLE III
Average Tip Radii Calculated by Taking the Mean Values of Tip Radii from Time Equal to 3–10 × 10^6

		Pe = 0.000	Pe = 0.001	Pe = 0.002
Upstream tip	R	95	88	81
	$\mathrm{Pe_t}$	0.09	0.15	0.17
	σ^*	0.23	0.15	0.16
Downstream tip	R	95	125	123
	$\mathrm{Pe_t}$	0.09	0.06	0.07
	σ^*	0.23	0.27	0.25
Normal tip	R	95	95	124
	$\mathrm{Pe_t}$	0.09	0.10	0.10
	σ^*	0.23	0.23	0.19

Note. The parameters used in these simulations are: St = −0.35, Pr = 0.1, $A_s = 0.4$, zero inverse kinetic mobility, and equal material properties.

calculated by taking the mean values from time equal to 0.3–10 $\times$ 10^{12}. The upstream tip radius decreases as the inlet flow velocity increases, which is in good agreement with the trend reported in a number of experiments (see, for example, [30]). With $\mathrm{Pe_f} = 0.001$, the tip radius of the arm perpendicular to the flow remains unchanged. However, with $\mathrm{Pe_f} = 0.002$ this tip radius increases due to the strong effect of the flow on the growth of the perpendicular arm, as discussed for Fig. 12. The Peclet number of the upstream arm tip increases with increasing melt velocity, which is the trend seen in the experiments of Lee *et al.* [30] and predicted by the theory of Bouissou and Pelece [31]. The Peclet number of the arm perpendicular to the flow is essentially constant even for $\mathrm{Pe_f} = 0.002$. The downstream Peclet number decreases as the flow is introduced. The stability parameter σ^* of the upstream arm tip decreases due to the flow, as was also observed by Beckermann *et al.* However, increasing the flow further does not affect σ^*. The experiments of Yee *et al.* show that for high undercooling, which is the case in our simulation, σ^* becomes independent of the upstream flow velocity. For low undercooling, their results shows that σ^* increases as the upstream flow increases. The value of σ^* for the perpendicular tip with $\mathrm{Pe_f} = 0.0001$ is similar to its value with no flow. This is consistent with the experiments of Bouissou *et al.* [32], which show that perpendicular component of the flow does not affect the stability parameter σ^*. The decrease of σ^* for the arms growing perpendicular to the flow for $\mathrm{Pe_f} = 0.0002$ is likely to be a result of the increased mismatch between the preferred growth direction due to anisotropy and the upstream tilt due to the oncoming flow.

Figures 13 and 14 show the void fraction and the rate of heat release, respectively, as a function of time for $\mathrm{Pe_f} = 0.0, 0.001$, and 0.002. As expected, larger inlet velocity leads to a

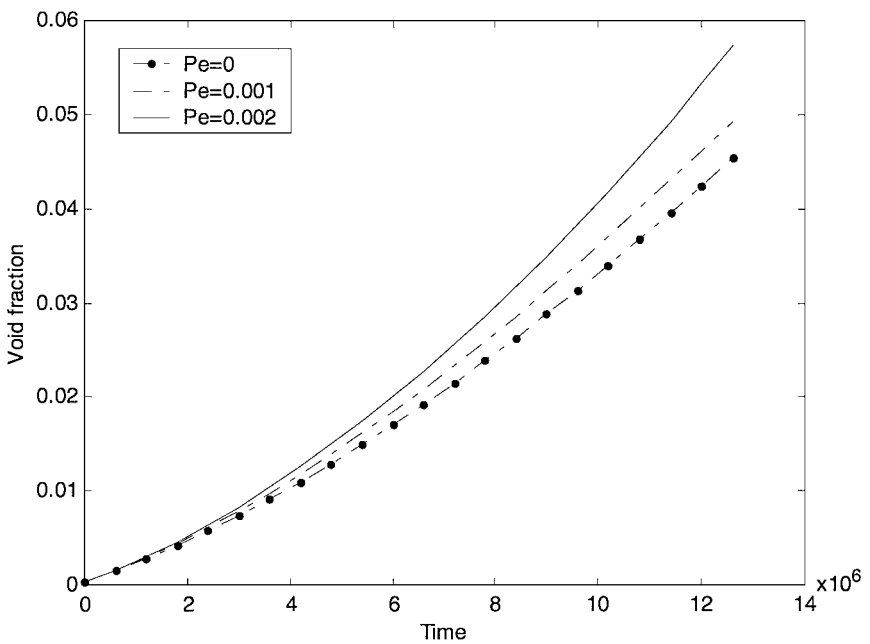

FIG. 13. The effect of Peclet number on the void fraction. The Peclet numbers used in the simulations are $\mathrm{Pe} = 0.0$, 0.001, and 0.002. The other parameters used in these simulations are $\mathrm{St} = -0.35$, $\mathrm{Pr} = 0.1$, $\mathrm{Pe} = 0.0$ (no flow), $A_s = 0.4$, zero inverse kinetic mobility, and equal material properties.

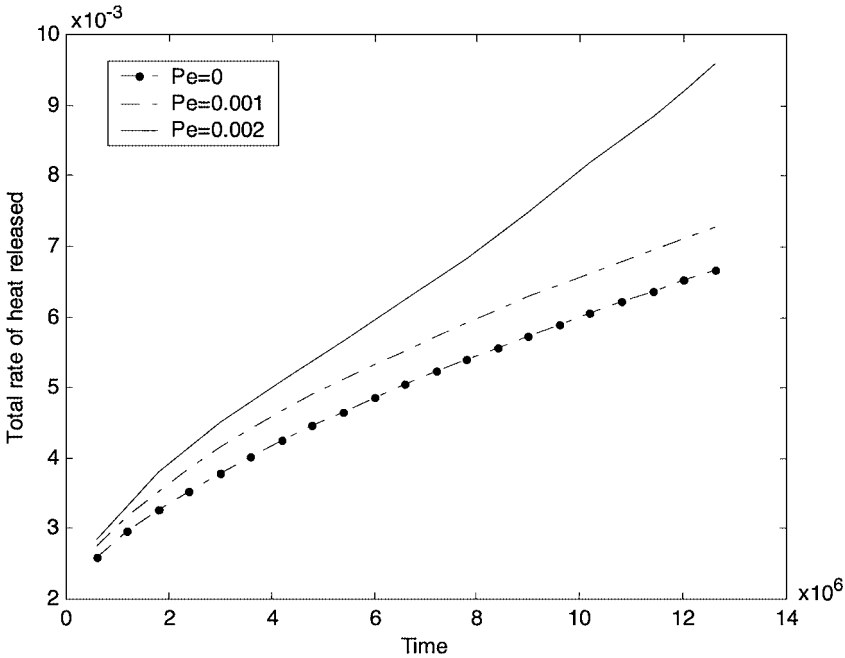

FIG. 14. The effect of Peclet number on the total rate of heat released. The Peclet numbers used in the simulations are Pe = 0.0, 0.001, and 0.002. The other parameters used in these simulations are St = −0.35, Pr = 0.1, Pe = 0.0 (no flow), $A_s = 0.4$, zero inverse kinetic mobility, and equal material properties.

faster growth. A higher Peclet number results in improved heat convection in the melt, more heat is released from the interface, and the solid, consequently, grows faster. The effect of the circulating wake for $\mathrm{Pe_f} = 0.002$ is clear by the significant increase in the rate of heat release. This increase in the heat release rate coincides with an increase in the downstream tip velocity, as shown in Fig. 12.

5.3. *The Effect of Prandtl Number on the Growth of Many Dendrites*

In practical situations, many dendrites usually grow close to each other. The interaction between the dendrites and between the dendrites and the flow affect the growth. We now examine the growth of many dendrites by a set of three simulations. Initially, the undercooled melt is seeded with 13 small solids. The parameters are St = −0.25, $A_s = 0.4$, zero inverse kinetic mobility, and equal material properties. Here we set $m = 4$ and use random values of θ_o resulting in fourfold dendrites with random preferred directions of growth. Simulation A is for no melt flow. In simulation B, $\mathrm{Pe_f} = 0.001$ and Pr = 0.1. In simulation C, the Prandtl number is increased to Pr = 10, keeping $\mathrm{Pe_f} = 0.001$.

Figure 15 shows the front and the isotherms for simulation A—growth without melt flow—at time equal to 24×10^6. The contours represent temperature isotherms of −0.02, −0.06, −0.08, −0.1, −0.15, −0.2, and −0.2475. Here the dotted line is for temperature −0.02, the dashed–dotted line is for temperature −0.1, and the dashed line is for the thermal boundary layer with a temperature of −0.2475. The dendrite arms facing away from the other dendrites grow with similar growth rate and slightly faster than the arms facing the other dendrites. At the time shown, no side branches have appeared.

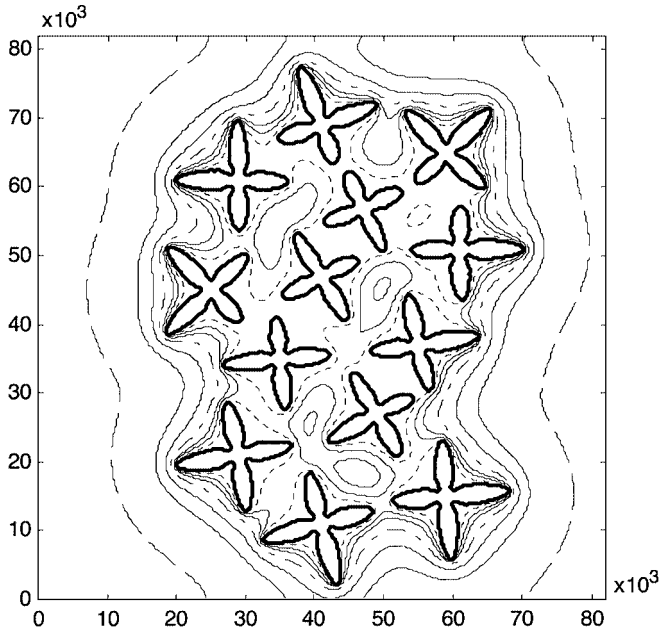

FIG. 15. Temperature contours around 13 dendrites growing close to each other at a nondimensional time equal to 24×10^6. The parameters used in this simulation are $\mathrm{St} = -0.25$, $\mathrm{Pe} = 0.0$ (no flow), $\mathrm{Pr} = 0.1$, $A_s = 0.4$, zero inverse kinetic mobility, and equal material properties.

Figures 16a and 16b show the temperature and the velocity fields, respectively, around the dendrites for simulation B at time 26×10^6. The flow results in higher upstream tip velocities, with the formation of side branches and lower downstream tip velocities due to the smaller temperature gradient. The growth rate of the dendrite arms located in

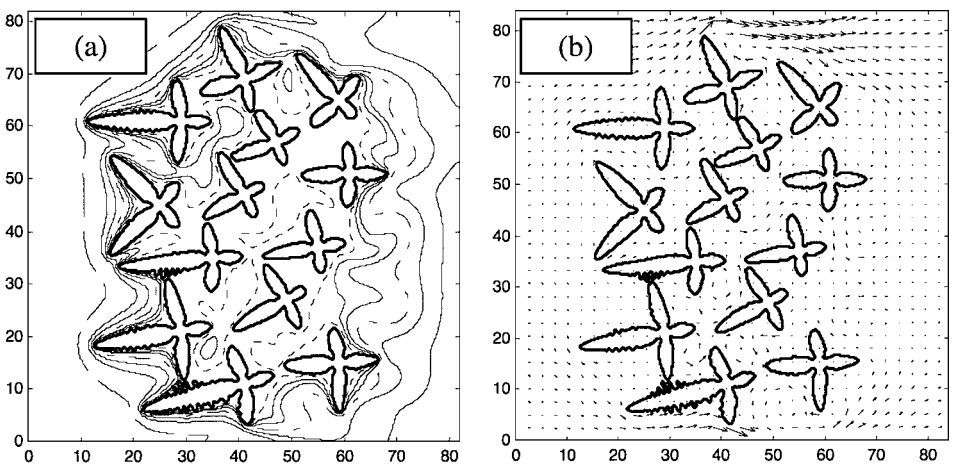

FIG. 16. Thirteen dendrites growing close to each other at a nondimensional time equal to 24×10^6. (a, b) Temperature contours and velocity field, respectively, around the dendrite. The parameters used in this simulation are $\mathrm{St} = -0.25$, $\mathrm{Pe} = 0.001$, $\mathrm{Pr} = 0.1$, $A_s = 0.4$, zero inverse kinetic mobility, and equal material properties. The axis values are multiplied by 10^{-3}.

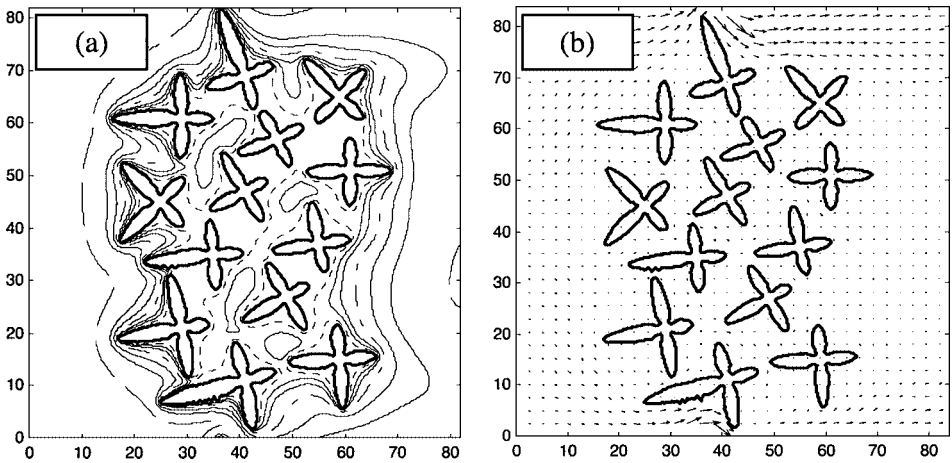

FIG. 17. Thirteen dendrites growing close to each other at a nondimensional time equal to 24×10^6. (a, b) Temperature contours and velocity field, respectively, around the dendrite. The parameters used in this simulation are $\mathrm{St} = -0.25$, $\mathrm{Pe} = 0.001$, $\mathrm{Pr} = 10$, $A_s = 0.4$, zero inverse kinetic mobility, and equal material properties. The axis values are multiplied by 10^{-3}.

the inner region and facing the flow direction increases and a few side branches start to form.

Figure 17 shows the temperature (left) and the velocity fields (right) around the dendrites for simulation C at time 26×10^6. As a result of the much higher Prandtl number, 100 times

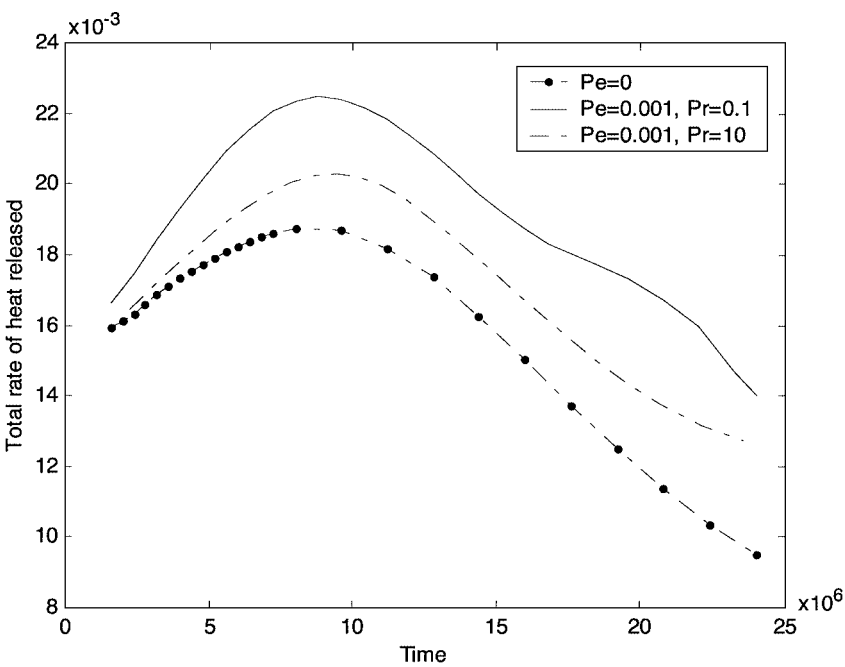

FIG. 18. The effect of Peclet number and Prandtle number on the total rate of heat released. The Peclet and Prandtl numbers used in the simulations are $\mathrm{Pe} = 0.0$ and 0.001 and $\mathrm{Pr} = 0.1$ and 10. The other parameters used in these simulations are $\mathrm{St} = -0.25$, $A_s = 0.4$, zero inverse kinetic mobility, and equal material properties.

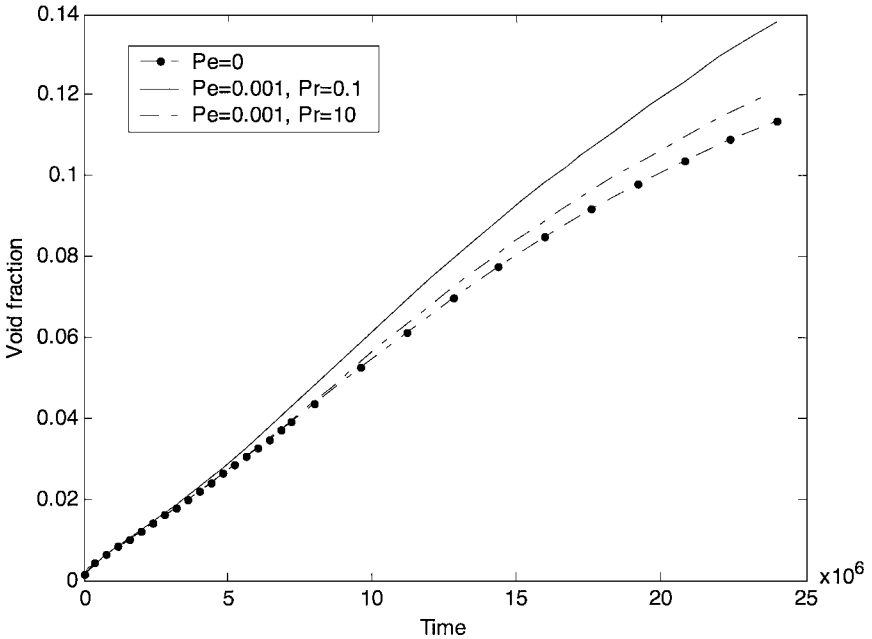

FIG. 19. The effect of Peclet number and Prandtl number on the void fraction. The Peclet and Prandtl numbers used in the simulations are Pe $= 0.0$ and 0.001 and Pr $= 0.1$ and 10. The other parameters used in these simulations are St $= -0.25$, $A_s = 0.4$, zero inverse kinetic mobility, and equal material properties.

the one used in simulation B, the flow has less effect on the temperature field. The temperature gradient on the upstream side is lower than the gradient in simulation B, resulting in a lower increase in the upstream tip velocities and fewer side branches. A similar effect is noticed in the inner region and for the downstream arms.

Figures 18 and 19 show the total rate of heat released and the solid fraction, respectively, as function of time for simulations A, B, and C. An increase in the flow rate results in a higher heat transfer from the interface, resulting in a higher solidification rate. A higher Prandtl number reduces the effect of the velocity on the heat transfer and the growth rate. The total rate of heat released increases initially and then starts to decrease. This decrease shows the effect of the dendrites growing close to each other.

6. CONCLUSIONS

We have presented a two-dimensional front tracking method for the simulation of dendritic growth with convection. The simulations showed that introducing melt flow results in an increase in growth rate of the arm growing into the flow, promoting more side-branch formation on the upstream side, and tilting the tip of the dendrite arm growing perpendicular to the flow toward the upstream direction. The flow also results in a reduction of the growth rate of the downstream arm. However, when the wake structure changes so that the fluid flows toward the tip, the velocity of this tip starts to increase. When many dendrites grow close to each other the effect of the flow on each dendrite depends on its position with respect to the flow direction and its position with respect to the other dendrites. Overall, the flow results in more heat release, faster growth rate, and more side-branch formation. The effect

of the flow increases with increasing flow Peclet number and decreasing Prandtl number. These results are in good agreement with experimental observations, but three-dimensional simulations are needed for complete quantitative results.

Numerical simulations of the effect of flow on the formation of microstructure is a very new development. However, progress is rapidly being made. The approach taken here is very similar to the front tracking computations of Shin and Juric [15], except that they included the solid region as a high-viscosity fluid whereas we force the velocity in the solid to be exactly zero. The method also has some similarity to the phase-field simulations of Tonhardt and Amberg [11] and Beckermann *et al.* [12], except that here the phase boundary is modeled directly with marker points. While these simulations are still limited to two-dimensional flows and relatively simple materials, more-complex three-dimensional simulations are likely to become commonplace within a few years (Al-Rawahi and Tryggvason [33]).

ACKNOWLEDGMENTS

Al-Rawahi thanks Sultan Qaboos University for financial support. This research was also supported in part by NASA grant NAG3-2583. We thank Dr. Bernard Bunner for many helpful discussions and for the use of his multigrid code to solve the pressure equation.

REFERENCES

1. M. E. Glicksman and S. C. Huang, Convective heat transfer during dendritic growth, in *Convective Transport and Instability Phenomena*, edited by J. Zierep and H. Ortel, Jr. (Braun, Karlsruhe, 1982), p. 557.
2. J. Strain, A boundary integral approach to unstable solidification, *J. Comput. Phys.* **85**, 342 (1989).
3. J. A. Sethian and J. Strain, Crystal growth and denditic solidification, *J. Comput. Phys.* **98**, 231 (1992).
4. A. A. Wheeler, B. T. Murray, and R. J. Scaefer, Computation of dendrites using a phase field model, *Physica D* **66**, 243 (1993).
5. R. Almgren, Variational algorithm and pattern formation in dendritic solidification, *J. Comput. Phys.* **106**, 337 (1994).
6. D. Juric and G. Tryggvason, A front tracking method for dendritic solidification, *J. Comp. Phys.* **123**, 127 (1996).
7. R. Kobayashi, A numerical approach to three-dimensional dendritic solidification, *Exp. Math.* **3**, 59 (1994).
8. A. Karma and W.-J. Rappel, Numerical simulation of three-dimensional dendritic growth, *Phys. Rev. Lett.* **77**(19), 4050 (1996).
9. A. Schmidt, Computation of three-dimensional dendrites with finite element, *J. Comp. Phys.* **125**, 293 (1996).
10. M. Plapp and A. Karma, Multiscale finite-difference-diffusion Monte-Carlo method for simulating dendritic solidification, *J. Comput. Phys.* **165**(2), 592 (2000).
11. R. Tonhardt and G. Amberg, Phase-field simulation of dendritica growth in a shear flow, *J. Crystal Growth* **194**, 406 (1998).
12. C. Beckermann, H.-J. Diepers, I. Steinbach, A. Karma, and X. Tong, Modeling melt convection in phase-field simulations of solidification, *J. Comput. Phys.* **154**, 468 (1999).
13. E. Bansch and A Schmidt, Simulation of dendritic crystal growth with thermal convection, *Interfacial Free Boundaries* **2**, 95 (2000).
14. D. Juric, Direct numerical simulation of solidification microstructures affected by fluid flow, in *Molding of Casting, Welding and Advanced Solidification Processes VIII*, edited by B. G. Thomas and C. Beckermann (The Mineral, Metals & Materials Society (TMS), Warrendale, PA, 1998), p. 605.
15. S. W. Shin and D. Juric, Computation of microstructure in solidification with fluid convection, *J. Mech. Behav. Mater.* **11**, 313 (2000).
16. J. A. Viecelli, A method for including arbitrary external boundaries in the MAC incompressible fluid computing technique, *J. Comput. Phys.* **4**, 543 (1969).

17. D. Goldstein, R. Handler, and L. Sirovich, Modeling a no-slip flow boundary with an external force field, *J. Comput. Phys.* **105**, 354 (1993).
18. E. M. Saiki and S. Biringen, Numerical simulation of a cylinder in uniform flow: Application of a virtual boundary method, *J. Comput. Phys.* **123**, 450 (1996).
19. M.-C. Lai and C. S. Peskin, An immersed boundary method with formal second-order accuracy and reduced numerical viscosity, *J. Comput. Phys.* **160**, 705 (2000).
20. E. A. Fadlun, R. Verzicco, P. Orlandi, and J. Mohd-Yusof, Combined immersed-boundary finite-difference methods for three-dimensional complex flow simulations, *J. Comput. Phys.* **161**, 35 (2000).
21. T. Ye, R. Mittal, H. S. Udaykumar, and W. Shyy, An accurate cartesian grid method for viscous incompressible flows with complex immersed boundaries, *J. Comput. Phys.* **156**, 209 (1999).
22. H. S. Udaykumar, R. Mittal, P. Rampunggoon, and A. Khanna, A sharp interface Cartesian method for simulating flows with complex moving boundaries, *J. Comput. Phys.* **174**, 345 (2001).
23. A. Karma and W.-J. Rappel, Phase-field method for computationally efficient modeling of solidification with arbitrary interface kinetics, *Phys. Rev. E* **53**(4), 3017 (1996).
24. M. Muschol and H. Z. Cummins, Surface-tension-anisotropy measurements of succinonitrile and pivalic acid—comparison with microscopic solvability theory, *Phys. Rev. A* **46**(2), 1038 (1992).
25. G. Tryggvason, B. Bunner, A. Esmaeeli, D. Juric, N. Al-Rawahi, W. Tauber, J. Han, S. Nas, and Y.-J. Jan, A front tracking method for the computations of multiphase flow, *J. Comput. Phys.* **169**, 708 (2001).
26. C. S. Peskin, Numerical-analysis of blood-flow in heart, *J. Comput. Phys.* **25**, 220 (1977).
27. H. S. Carslaw and C. J. Jaeger, *Conduction of Heat in Solids*, 2nd ed. (Clarendon, Oxford, 1959).
28. J. Drummond and M. Tahir, Linear viscous flow through regular arrays of parallel solid cylinders, *Int. J. Multiphase Flow* **10**(5), 515 (1984).
29. A. Sangani and A. Acrivos, Slow flow through a periodic array of spheres, *Int. J. Multiphase Flow* **8**(4), 343 (1982).
30. Y.-W. Lee, R. Ananth, and W. N. Gill, Selection of length scale in unconstrained dendritic growth with convection in the melt, *J. Crystal Growth* **132**, 226 (1993).
31. Ph. Bouissou and P. Pelece, Effect of forced flow on dendritic growth, *Phys. Rev. A* **40**(11), 6673 (1989).
32. Ph. Bouissou, B. Perrin, and P. Tabeling, Influence of an external flow on dendritic crystal growth, *Phys. Rev. A* **40**(1), 509 (1989).
33. N. Z. Al-Rawahi and G. Tryggvason, The effect of fluid flow on dendritic solidification, in *The Proceedings of the Fourth International Conference on Multiphase Flow* (*ICMF*), edited by E. E. Michaelides (Tulane University, New Orleans, LA, 2001), No. 408.